ACS Photonics

Open Access

pubs.acs.org/journal/apchd5

Article

Quantitative Assessment of Collagen Remodeling during a Murine Pregnancy

Jessica C. Ramella-Roman,* Mala Mahendroo, Clothilde Raoux, Gaël Latour, and Marie-Claire Schanne-Klein*

Cite This: *ACS Photonics* 2024, 11, 3536−3544

Read Online

ACCESS | Metrics & More | Article Recommendations | Supporting Information

ABSTRACT: Uterine cervical remodeling is a fundamental feature of pregnancy, facilitating the delivery of the fetus through the cervical canal. Yet, we still know very little about this process due to the lack of methodologies that can quantitatively and unequivocally pinpoint the changes the cervix undergoes during pregnancy. We utilize polarization-resolved second harmonic generation to visualize the alterations the cervix extracellular matrix, specifically collagen, undergoes during pregnancy with exquisite resolution. This technique provides images of the collagen orientation at the pixel level (0.4 μm) over the entire murine cervical section. They show tight and ordered packing of collagen fibers around the os at the early stage of pregnancy and their disruption at the later stages. Furthermore, we utilize a straightforward statistical analysis to demonstrate the loss of order in the tissue, consistent with the loss of mechanical properties associated with this process. This work provides a deeper understanding of the parturition process and could support research into the cause of pathological or premature birth.

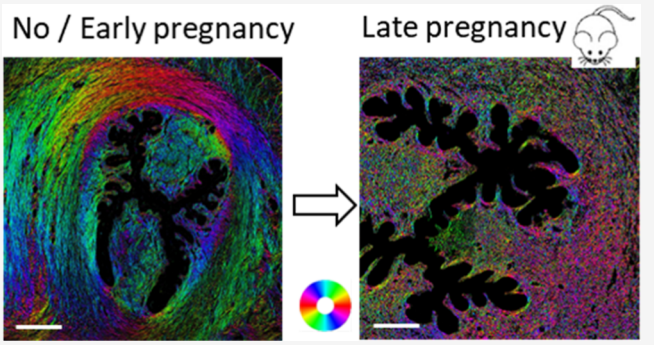

KEYWORDS: *second harmonic generation microscopy, polarimetry, multiphoton imaging, collagen, uterine cervix*

INTRODUCTION

Preterm birth (PTB) is the leading cause of infant mortality worldwide. PTB also leads to lifelong morbidities and accounts for an estimated 69 million disability-adjusted life years annually worldwide (Global Disease Burden Study, 2019). In the United States, 1 in 10 babies is born premature,[1−3] and inequalities in the access and quality of prenatal care[4] and other social determinants of health[5,6] contribute to some of the highest levels of PTB in underserved groups.[7] Cervical remodeling, the process by which the cervix transforms from a closed rigid structure to a compliant structure that can allow safe passage of the fetus, is an essential feature of normal parturition. In spontaneous preterm birth (sPTB), which accounts for around 80% of PTBs,[8−12] the remodeling process is accelerated,[13,14] and approximately 25% of pregnancy losses that occur during the fourth to sixth month of pregnancy happen because of a prematurely weakened cervix. Early identification of pathological or accelerated cervical remodeling would allow clinicians to improve the design of drug trials for prevention and start a course of treatment or monitoring that could significantly improve the baby's health outcomes.

In both women and animal models, the phases of cervical remodeling during pregnancy can be described as cervical softening, ripening, and dilation. These phases are associated with changes in the cervix's mechanical properties, which relate strongly to changes in the cervical collagen and fibrous tissue directionality, dispersion, cross-link density, and turnover, as shown by Myers and others.[8−12,15−17] The cervix comprises a rich extracellular matrix within the stroma, which lies under an epithelium, and collagen fibers are a major constituent.[18−21] In early pregnancy, collagen remains in an organized fibrous structure. As gestational age advances, the cervix becomes softer[12,22] due to the structural reorganization of collagen in the stroma.[11,23,24]

Numerous researchers have studied cervical collagen[17,25−31] and its anisotropic alignment surrounding the cervical canal[9,10,16,32] through a variety of techniques, including magnetic tensor imaging,[33] quantitative ultrasound,[34] optical coherence tomography,[35] and Mueller matrix polarimetry.[36−38] Raman spectroscopy showed an apparent decrease in collagen type I peaks over the normal pregnancy period.[39] Other studies have utilized second harmonic generation (SHG) microscopy to observe cervical remodeling in mice[40−42] as SHG has

Received: February 23, 2024
Revised: July 23, 2024
Accepted: July 29, 2024
Published: August 14, 2024

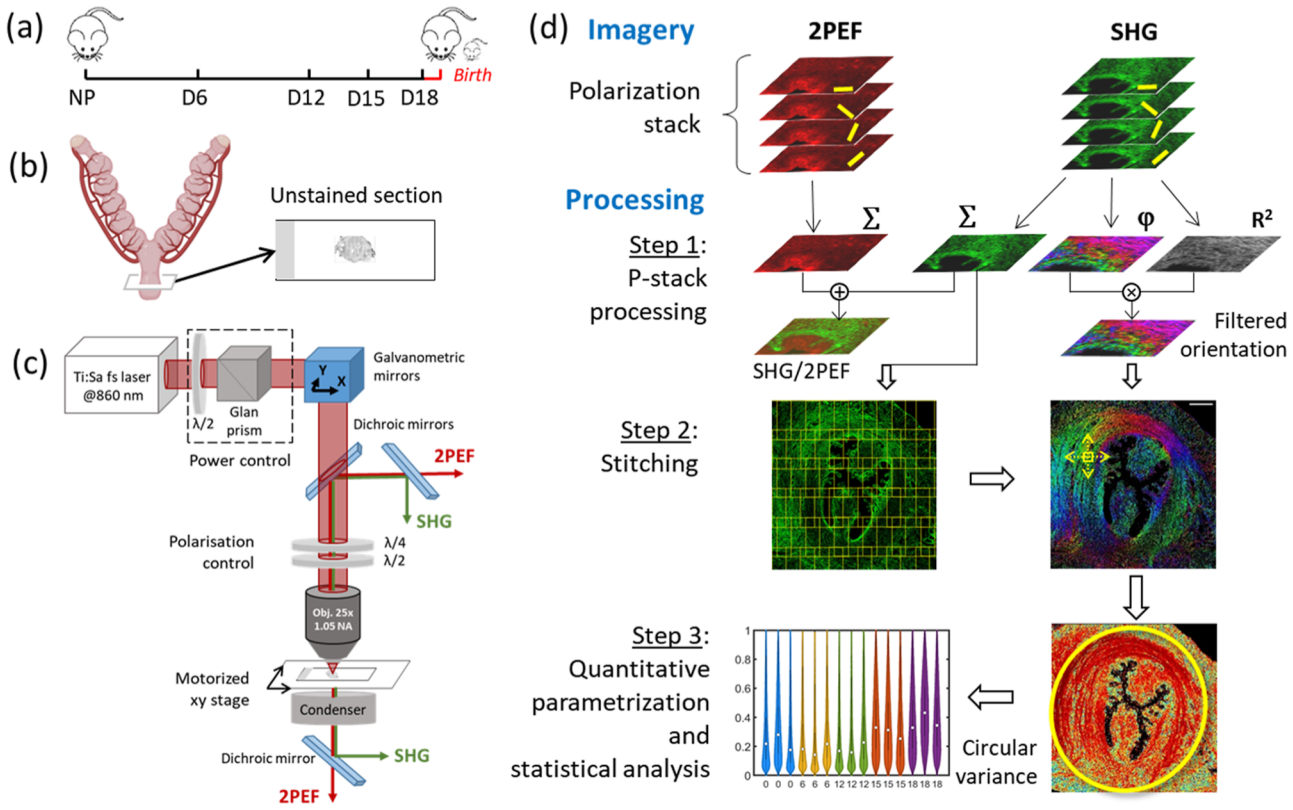

Figure 1. Full process of cervical remodeling characterization. (a) Timeline of murine pregnancy and stages under study. Delivery is on gestation day 19. (b) Schematic of the uterus and cervix indicates tissue sectioning perpendicular to the cervical canal. (c) Laser-scanning multiphoton microscopy with parallel trans- and epi-detection of 2PEF and SHG signals. Polarization is controlled by a quarter- and a half-waveplate. The sample is on a motorized stage to scan large regions. (d) Imagery and image processing workflow: step 1: polarimetric image stacks are processed automatically to provide I_{2PEF} and I_{SHG} images as well as R^2-filtered in-plane orientation φ maps; step 2: all the tiles are stitched together starting from the I_{SHG} image (see the superimposed grid in the SHG image); step 3: order metrics are computed in small regions of interest (see yellow lines in the orientation map) all over the stitched orientation image and the distribution of the order metrics around the os (within the yellow elliptical mask) are analyzed for every mouse.

unmatched specificity to fibrillar collagen and provides a direct visualization without any labeling.[43−45] Mahendroo et al. have shown that collagen bundles lose their characteristic elongated appearance during the softening phase in favor of a more kinked one; they also become thicker with the progression of gestation.[11] Nevertheless, no accurate quantification of collagen remodeling during pregnancy has been reported due to limitations in spatial resolution, specificity to collagen, or sensitivity to orientation of all of these techniques.

This study uses polarization-resolved SHG (p-SHG) microscopy to map and assess collagen remodeling during pregnancy. P-SHG consists of recording SHG images for a series of different linear polarizations of the laser excitation. This technique's unique feature is the ability to directly quantify the orientation of collagen fibers' primary axis at the pixel level (420 nm)[46−51] without the use of interpretative or contrast-based algorithms commonly used in SHG imaging.[52,53] As such, p-SHG is used to observe collagen remodeling during pregnancy with unmatched spatial resolution. This modality is combined with two-photon-excited fluorescence microscopy (2PEF) from endogenous cellular chromophores in unstained sections, yielding mapping of the cervix morphology. From p-SHG data, we have created collagen orientation maps of the entire murine cervix and have used metrics of order, such as circular variance, entropy, and kurtosis, to observe the changes in the extracellular matrix architecture at four time points in the 19 day mouse gestation and in nonpregnant (NP) mice. This new study provides evidence of a significant disorganization of collagen between the early and late stages of pregnancy in our murine model.

RESULTS

Multiphoton images of unstained cervical sections of NP mice and mice at gestation days 6 (D6), 12 (D12), 15 (D15), and 18 (D18) are recorded and processed as shown in Figure 1. A combined 2PEF/SHG image acquired with submicrometer resolution over the total size of a D6 murine cervix is shown in Figure 2a. In this representative D6 sample, the internal cervical os is visible around a central region with no SHG or 2PEF signal. The strong 2PEF signal (red color) is due to endogenous cellular chromophores (NAD(P)H, FAD, etc.)[54] that reveal the epithelial cells delineating the cervical os. The SHG signal (green color) shows the collagen fibers around the os. A stronger SHG signal is observed near the epithelial cells around the os, which reveals a high density of well-aligned collagen fibers. The collagen fibers away from the os exhibit a circumferential organization. An accurate orientation of the fibers cannot be visualized clearly because of the high density of the collagen network. This limitation is overcome when using the pSHG modality, as shown in Figure 2b, which provides the orientation of the collagen fibers in every pixel. This orientation map shows that the collagen fibers away from

https://doi.org/10.1021/acsphotonics.4c00337
ACS Photonics 2024, 11, 3536−3544

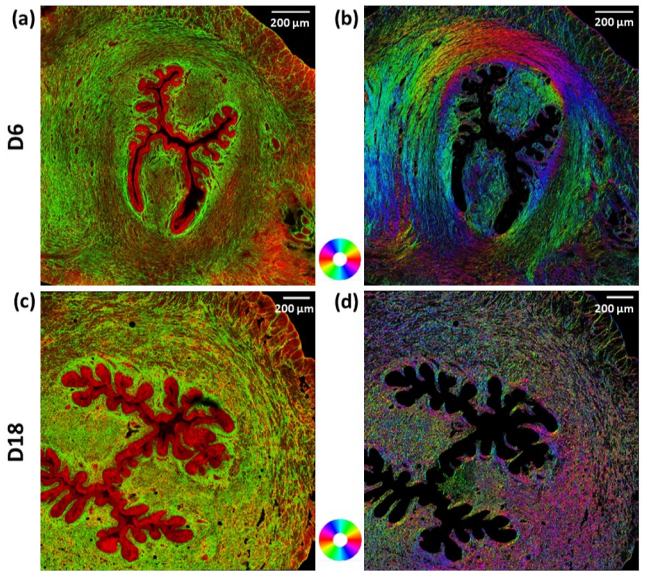

Figure 2. 2PEF/pSHG images of murine cervices at gestation days 6 and 18. (a,c) Combined I_{2PEF} (red color) and I_{SHG} (green color) images showing the morphology of the cervix at D6 (a) and D18 (c). 2PEF is obtained from endogenous cellular chromophores. SHG reveals collagen fibers. (b,d) Orientation map of collagen fibers extracted from pSHG data from the same samples as in (a) and (c). HSV look-up table is used: H codes the collagen orientation as shown by the color wheel (red color means horizontal, cyan color means vertical), $S = 1$ and $V = R^2$ for $R^2 > 0.5$, $V = 0$ otherwise.

the os are well aligned with a tangential direction around the os. In contrast, the collagen close to the os is primarily oriented toward the os.

Figure 2c,d displays similar data for a D18 murine cervix that is 1 day before birth. Consistent with cell proliferation and tissue growth during pregnancy, the cervix is larger on gestation day 18.[55] Second, the orientation map in Figure 2d demonstrates a marked change in the distribution of collagen with a random distribution of collagen fibers throughout the cervix, in contrast to the well-aligned fibers seen on D6 (Figure 2b). Note that the raw SHG images in Figure 2a,c do not enable us to differentiate the fiber distributions in the D6 and D18 samples because the collagen density remains high in the D18 sample. Notably, the pSHG map (Figure 2d) shows that the apparent organization of collagen around the os in the raw SHG image (Figure 2c) that corresponds to collagen packing, not to the collagen overall orientation.

Similar patterns are obtained in the other D6 and D18 samples. Moreover, 2PEF/SHG images and orientation maps recorded in NP and D12 samples are similar to those in the D6 sample. In contrast, by gestation day D15, the random distribution of collagen as in D18 samples becomes evident (see Supporting Information Figures S1 and S2).

For further quantitative analysis of the collagen orientation maps, metrics of order such as statistical entropy, circular variance, and kurtosis are calculated in regions of interest (ROI) of size 10×10 pixels (4.2×4.2 μm^2) spanning the full cervix. The entropy and the variance are equal to 1 when the orientation distribution in the ROI is completely random, while they are 0 for a perfectly ordered distribution with a

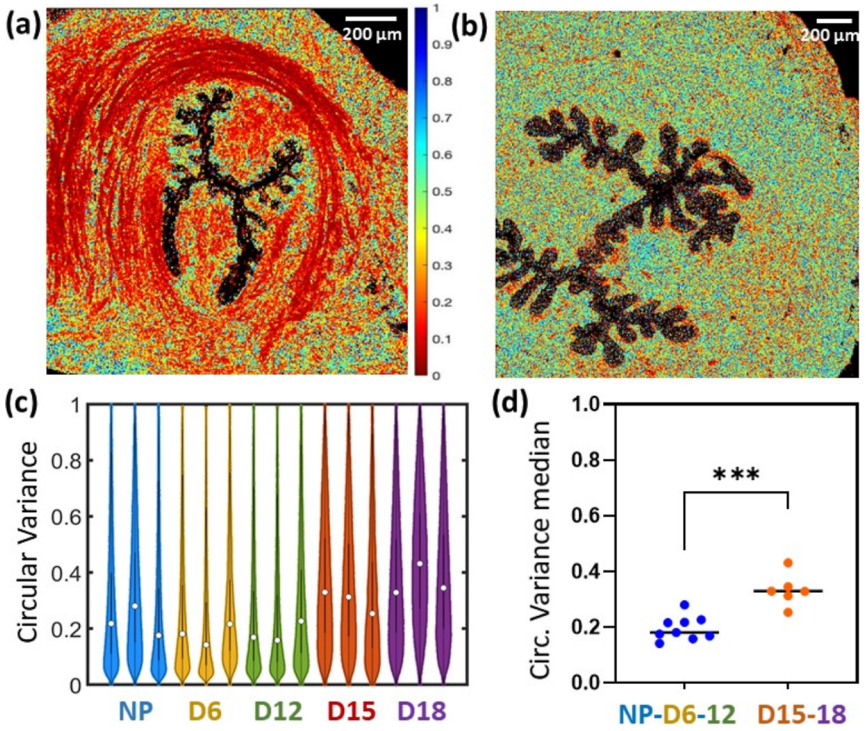

Figure 3. Order metrics of collagen orientation. The circular variance is 0 for a perfectly ordered distribution and 1 for a completely random one. (a,b) Map of the circular variance calculated in small ROIs spanning the pSHG orientation image of the same (a) D6 and (b) D18 samples as in Figure 2. (c) Violin plots of the circular variance calculated in all the ROIs spanning the cervix for all samples under study. Each column represents a different sample from a different mouse. Median (white dot) and interquartile line (black bold line) are plotted for every column. In every sample, the edges are eliminated by an elliptical mask covering the os. (d) Median circular variance of the groups NP, D6 and D12 ($n = 9$) and D15 to D18 ($n = 6$). Welch's t-test shows a significant difference ($p = 0.0009$).

https://doi.org/10.1021/acsphotonics.4c00337
ACS Photonics 2024, 11, 3536−3544

unique orientation. Accordingly, maps of the circular variance show lower values in the D6 sample than in the D18 sample (Figure 3a,b). The same trend is observed for the entropy (Supporting Information Figure S3a,c), while the kurtosis is higher in the D6 sample (Supporting Information Figure S3b,d) and the skewness is close to zero in all samples (Table S1).

The results for all samples (NP, D6, D12, D15, and D18) are summarized in Figure 3c,d. The violin plots display the values of the circular variance calculated for every murine sample in all of the ROIs spanning the cervix, after elimination of the edges by an appropriate elliptical mask covering the os. These violin plots show median variance values of 0.2 or lower for NP, D6 and D12 samples, while for D15 and D18, variance values are at 0.3 or above. The distribution is also broader in the late stage of pregnancy compared to that in the early stages of pregnancy. Similar trends are observed for other metrics, such as entropy and kurtosis, shown in Figure S3. In the Supporting Information, we also show the entire imaged set (Figures S1 and S2).

Finally, Welch's t tests are performed on the median values of these order metrics (Figure 3d). They show that the median circular variance at the early stage of pregnancy (D0 + D6 + D12) is significantly different from the one at late stages of pregnancy (D15 + D18) ($p = 0.0009$). A significant difference is also found for the entropy ($p = 0.0065$) and the kurtosis ($p = 0.0004$), as shown in Supporting Information Figure S3e,f.

DISCUSSION

In this study, we have recorded multimodal multiphoton images of an unstained murine cervix at different stages of gestation utilizing pSHG and 2PEF. Combining 2PEF images of cellular chromophores with SHG images of collagen fibers provides a clear visualization of the cervix morphology at submicrometer resolution. Applying p-SHG to obtain direct visualization of collagen orientation in each pixel provides unique insights into spatial variations in collagen orientation at a previously unachieved resolution. The application of this novel methodology holds the potential to identify regional variations in the pattern of collagen remodeling during gestation without the use of algorithms based on contrast and Fourier transform, often used with SHG microscopy. In NP mice, as well as before 12 days of gestation, the collagen fibers are well organized, aligning along the circumference of the os. Regional variations exist as collagen fibers in the subepithelia stroma region near the os show a different organization, following the edges of the folds. At the late stages of gestation, i.e., from 15 days of gestation, the distribution of the collagen fibers changes abruptly: they show a random organization.

These qualitative observations of cervix remodeling during gestation call for a quantitative measurement of collagen distribution. Collagen visualization in small cervical tissue samples has been accomplished with hydroxyproline titration, and such measurements have indicated a constant collagen content through pregnancy.[55] However, this is a lengthy and specialized process that still requires the identification and classification of collagen fibers. Quantitative analysis of the raw SHG images has also been used in this context[41] but it is a complex issue. First, the SHG intensity alone is not considered a robust metric because of this modality's coherent and nonlinear nature.[44,56,57] Second, quantification of the collagen distribution in the field of view by appropriate image processing is affected by the high density of the collagen network in the cervix, which hinders the segmentation of individual fibers or the analysis of their direction on scales smaller than a few micrometers. For instance, a combination of SHG microscopy with Fourier transform analysis can provide orientations of collagen in rat cervix only in ≈25 μm-sized regions.[42,45]

To overcome these limitations, we have acquired pSHG images and used a processing workflow to automatically extract collagen orientation in every pixel of 420 nm size. The basic principle of this method is that the SHG signal is larger for incident polarization parallel to the fibrils than for incident polarization perpendicular to the fibrils. Recording a series of images with different incident polarizations then provides the main orientation of the collagen fibrils in every voxel, independently of the neighboring voxels. The advantage of this approach is the establishment of orientation maps with improved resolution compared to other techniques, including optical techniques like Mueller matrix polarimetry[36,37,58,59] or optical coherence tomography.[35] The latter techniques are not specific for collagen, resulting in a strong image background. Mueller matrix polarimetry thus uses large pixel size (>10 μm) to improve the signal-overnoise ratio, while the OCT resolution is also a few micrometers. In contrast, pSHG imaging is specific for collagen, and its low background translates into high sensitivity.[43,44,54] Moreover, the orientation of the collagen fiber in every voxel is determined in a ratiometric way, which is highly robust. Therefore, the pSHG orientation maps are reliable data, which cannot be affected by any subtle variation in the imaging conditions or tissue preparation. Accordingly, pSHG orientation maps uniquely show the collagen orientation distribution in the cervix at submicrometer resolution. However, pSHG is a slow technique since it requires acquiring several images upon different incident polarization orientations. From this point of view, advanced image processing techniques may be an interesting trade-off between resolution and imaging speed.[53] Alternately, advanced implementation of pSHG can improve the speed of pSHG acquisition.[60,61]

Order metrics are processed in small ROIs spanning the cervix for quantitative analysis, offering an unbiased view of the cervix structure. We compute the statistical entropy and the circular variance, which both increase with disorder and are equal to 0 for a perfectly ordered distribution and 1 for a random distribution; we also use circular kurtosis (respectively skewness) that is higher when the distribution is more tailed (respectively asymmetric). In NP mice and the early gestation stages, the collagen fibers' circumferential orientation is observed, and the circular variance is relatively low, confirming that collagen fibers are very well ordered, with low dispersion around the main direction. Interestingly, pSHG images do not show areas of preferential alignment in the anterior, posterior, right, or left quadrant of the cervix, as reported by Zork et al. and others.[8] The variance image indicates a narrowing in the packing in the superior and posterior zones, but this is believed to be due to the geometry of the cervix rather than other forces. A different collagen organization is observed in the folds, closer to the os, where the circular variance is more significant, indicating a less ordered area. Other investigators have shown through histology that in this area, collagen is arranged longitudinally;[32] since our imaging is conducted *en face* and pSHG measures in-plane orientation, the longitudinal orientation of collagen is not well visualized here.

https://doi.org/10.1021/acsphotonics.4c00337
ACS Photonics 2024, 11, 3536−3544

When observing the timeline of pregnancy, a great deal of change occurs from day 12 to day 15 of gestation, with an almost complete loss of order in all metrics: the orientation map shows fine scattered fibers in every color, and the circular variance image shows higher values over all of the entire cervix. This difference is highlighted in the violin plots, and statistical tests evidence a significant difference between the D15 and D18 mice, on one hand, and the NP, D6, and D12 mice, on the other hand, for all order metrics. This abrupt change of collagen distribution between D12 and D15 supports previous reports based on other techniques, which show an increase in cervix volume and dry mass and a decrease in collagen cross-links and apparent density.[10,55] These reports also show that these changes are associated with a loss of equilibrium stiffness from D6, with a stronger decrease of this mechanical property between D12 and D15.[10,55] These concordant timelines confirm that collagen remodeling toward a more disordered distribution is a key process enabling delivery. Importantly, our data further provide a quantitative metric of this collagen remodeling at a micrometer scale, which is not accessible by other techniques.

The structural changes in the cervix are inextricably linked to the changes in its mechanical properties and ability to maintain a growing fetus in utero. Several investigators have argued that a constitutive material model for cervical tissue inspired by its microstructure is needed to achieve a realistic model of cervical mechanical load distribution.[10] Structural parameters used in recently reported constitutive models include collagen orientation and dispersion.[62,63] Collagen orientation maps at the micrometer scale obtained by pSHG thus provide invaluable quantitative data on the anisotropy and heterogeneity of collagen structure and will facilitate improved design of an advanced constitutive model based on a more realistic description of the cervix microstructure.

Future work will focus on further understanding of both animal and human cervical remodeling with this new tool. In the animal model, there seems to be a bimodal behavior before and after day 12 of pregnancy that should be explored further. The remodeling rate is unknown and could be investigated with the appropriate timing of the experiments. Furthermore, how the remodeling propagates from the endo to the ectocervix could provide valuable information to researchers devising diagnostic devices for preterm labor diagnosis; this could be studied by probing the cervical tissue in-depth and further sectioning the cervix. The ability to obtain high-resolution and spatially defined structural collagen information can enhance understanding of premature cervical remodeling in mouse models of inflammation-induced or hormone-withdrawal-induced premature birth and with cervical insufficiency. Expanding this work to a human cervical sample will provide, for the first time, a clear characterization of the woman's cervical extracellular matrix at an unseen resolution. Although some have shown SHG images of the human cervix,[40−42] the addition of the angular orientation with pSHG can provide exquisite detail of spatially defined changes in collagen architecture. We anticipate the application of this novel methodology to the study of term and preterm cervical remodeling in animal models and humans holds future potential to develop improved tools for detecting and preventing PTB.

METHODS

Samples. Pregnant female mice, strain C57BL6/129sv, were utilized in this study. The time of pregnancy (day 0) was determined by observing a vaginal plug at the end of a 6 h breeding process that started in the morning of the same day. Mice delivered pups in the early morning on day 19. We followed the NIH Guide for the Care and Use of Laboratory Animals for all animal breeding procedures. The Institutional Animal Care and Use Committee reviewed and approved the research protocols at the University of Texas Southwestern Medical Center (IACUC 2016-101519) and at Florida International University (registration number: IACUC-20-014). All animals were maintained and used in accordance with ARRIVE guidelines.

In this study, we imaged the cervices of three NP mice and three mice at gestation day 6 (D6), at gestation day 12 (D12), at gestation day 15 (D15), and at gestation day 18 (D18) (Figure 1a). First, the mice cervices were snapped frozen at −80 °C in optimal cutting temperature compound (Tissue Tek, Elkhart, Indiana). A cryostat (Leica CM3050) was used for the transverse cryosectioning of the cervix at −20 °C. The cervical tissue sections were taken in the first 200 μm of uterine cervix starting from the end of the vaginal canal. They had a nominal thickness of 50 μm and were mounted on glass slides (Figure 1b).

P-SHG Imaging. Multimodal SHG/2PEF images were recorded using a custom-built upright laser scanning multiphoton microscope as previously described (Figure 1c).[64,65] Excitation was provided by a femtosecond titanium-sapphire laser (Mai-Tai, Spectra-Physics) tuned at 860 nm and scanned in the *XY* directions using galvanometric mirrors. Resolutions of 0.35 μm × 1.2 μm (fwhm, lateral × axial) and a field of view of 540 × 540 μm^2 were achieved using a high numerical aperture (NA) objective lens with water immersion (25×, NA 1.05, XLPLN-MP, Olympus). Excitation power at the sample was 5−10 mW. SHG and 2PEF signals were detected simultaneously in the epi- and trans-directions utilizing photon-counting photomultiplier tubes (P25PC, Electron tubes) and suitable spectral filters and dichroic mirrors to reject the excitation beam and select the SHG signal at 430 nm (FF01-680SP, FF01-720SP, FF01-427/10 Semrock) and the 2PEF signal in the 450−650 nm range (FF01-680SP, FF01-720SP Semrock, GG455, Schott). Because the SHG signal was larger than the 2PEF signal and trans-detection was more efficient than epi-detection, neutral densities (2 to 10-fold attenuation) were added on the trans-SHG channel to avoid photon counting saturation.

Polarimetric imaging was obtained by controlling the linear polarization of the incident field by an achromatic half-waveplate inserted in a motorized rotating mount at the back aperture of the objective (F102978, 30 mm diameter, Fichou). An achromatic quarter wave-plate (F102977, 30 mm diameter, Fichou) was inserted at the same place to optimize the linearity of the polarization. Series of 18 images were acquired every 10° between 0 and 170°, in a reduced field of view of 370 × 336 μm^2, using a pixel size of 420 nm and 5 μs pixel dwell time (total acquisition time around 15 s).

A motorized sample stage (PLS-XY/MCM3001, Thorlabs) was implemented to record a series of polarization-resolved images over the full section (around 2 × 2 mm^2). A snake motion pattern was used with 250 μm steps in the *X* and *Y*

https://doi.org/10.1021/acsphotonics.4c00337
ACS Photonics 2024, 11, 3536−3544

directions, i.e., with around 30% overlap between adjacent tiles. Typically 8 × 8 tiles were acquired over around 2.4 × 2.4 mm^2.

P-SHG Theoretical Analysis and Image Processing. The variation of the SHG signal as a function of the incident polarization can be described theoretically in the framework of tensorial nonlinear optics.[66] Detailed derivation can be found in the Supporting Information. Briefly, following previous reports, we consider here that the collagen fibrils exhibit a cylindrical symmetry and that the Kleinman symmetry is valid.[65] The second-order nonlinear susceptibility tensor $\chi^{(2)}$ of collagen then comprises only 2 independent components in the fibril frame and the SHG signal intensity of a collagen fibril oriented at angle φ to the X axis in the imaging plane writes as follows

$$I_{SHG}(\theta) = a_0 + a_2 \cos[2(\theta - \varphi)] + a_4 \cos[4(\theta - \varphi)] \quad (1)$$

Here, θ is the orientation of the incident polarization to the X axis and a_0, a_2, and a_4 are related to the collagen susceptibility, the collagen orientation out of the imaging plane XY, the square of the excitation intensity, as well as to other experimental parameters. Fourier analysis of $I_{SHG}(\theta)$ then provides 4 parameters (Figure 1d):

- The SHG signal averaged over all linear polarizations: $I_{SHG} = a_0$. This SHG intensity is similar to the usual SHG image acquired with circularly polarized excitation and same total acquisition duration. The 2PEF signal that is acquired simultaneously is processed the same way to get an averaged 2PEF signal similar to the one acquired without polarimetric modality: I_{2PEF}.
- The in-plane orientation φ of the collagen fibrils.
- A coefficient of determination R^2 that compares the experimental data and the curve obtained from the a_0, a_2, and a_4 Fourier parameters (see eq S5 in the Supporting Information). Indeed, the Fourier analysis provide angles even if the experimental data do not match the theoretical analysis at all. For instance, the cylindrical symmetry does not apply in voxels encompassing crossing fibrils. In this case, eq 1 is not valid anymore because of higher-order Fourier components and the φ angle determined from the second and fourth Fourier components is not reliable. Angles determined with $R^2 < 0.5$ are thus filtered out and depicted as black pixels in the images. $R^2 > 0.5$ are used to code the brightness in orientation maps. Quantitative analyses (see below) are performed only on pixels with $R^2 > 0.5$.
- The ratio of the 2 components of collagen $\chi^{(2)}$ in the microscope frame can also be obtained.[49,67] This parameter varies with the collagen out-of-plane orientation and the orientation disorder of the collagen fibrils within the focal volume. It is not directly informative in this study.

An automatic processing workflow was implemented using Matlab (MathWorks Inc.) to get I_{SHG} and I_{2PEF} images and R^2-filtered in-plane orientation φ maps for all of the tiles acquired in the same section (Figure 1d). The Fiji Plugin "Grid/collection stitching"[68] was then used to stitch together all the tiles (Figure 1d). It was first applied to the I_{SHG} tiles, and the configuration file was saved. A Matlab script was then used to load the single I_{2PEF} and φ images and collate them in the same way as the I_{SHG} images by use of the tile coordinates collected from the I_{SHG} configuration file. The stitched I_{SHG} and I_{2PEF} images were then merged by using false colors. The stitched orientation maps of the in-plane angle φ were depicted using an HSV look-up table: H codes the collagen orientation according to the color wheel in inset, $S = 1$ and $V = R^2$ for $R^2 > 0.5$, $V = 0$ otherwise.

Order Metrics and Statistical Analysis of the Orientation Maps. A statistical analysis was conducted for further quantitative mapping of the collagen orientation distribution (Figure 1d). The local orientation distributions were first computed in sliding ROIs all over the stitched orientation image. 10 × 10 pixels ROIs (4.2 × 4.2 μm^2) were used as the best trade-off between the spatial resolution and the precision of the statistical parameters. We also utilized ROIs of 5 × 5 pixels, which produced similar results, while larger ROIs lowered the resolution of the maps to an unacceptable level. The collagen organization was then quantified by computing the statistical entropy, the circular variance, the circular kurtosis, and the circular skewness of these local orientation distributions.[45,65,69] The latter parameters were computed using the circular statistics toolbox in Matlab.[69] Angles were first doubled to account for the [0−180°] range of orientation angles obtained from p-SHG. The statistical entropy was calculated as[65]

$$S = \frac{-1}{\ln[nb(\varphi)]} \sum_{\varphi=-90^\circ}^{90^\circ} p(\varphi)\ln[p(\varphi)] \quad (2)$$

Here, $p(\varphi)$ is the normalized number of pixels with the orientation ϕ in the image; the denominator is a normalization factor to be independent of the total number of angular bins $nb(\varphi)$ in the distribution.

Circular kurtosis, skewness, and variance are metrics similar to their non-circular counter-parts. The circular variance assesses the width of the orientation distribution of collagen, the circular kurtosis is a measure of the "tailedness" of this distribution, and the skewness is a measure of the asymmetry of this distribution. The entropy is a more general disorder metric that measures the disorder of any distribution, while the variance is more meaningful for single-peaked distributions.

Once the images of these order parameters were created, an elliptical mask was utilized to suppress pixels not belonging to the cervix, such as vaginal walls and other connective tissue. The size of the mask was dependent on the image, but we strived to accept 75% of the data starting from the center defined as a visible os. The selected pixels were then used to create the violin plots.

Finally, the group composed of early stage cervix samples NP, D6, and D12 and the one composed of D15 and D18 samples were compared using an unpaired t-test with Welch's correction. A p value less than 0.05 was considered as significant. Box plots show the median.

■ ASSOCIATED CONTENT

Data Availability Statement

Raw imaging data as well as processed orientation map and SHG/2PEF map of every cervical sample are available for download at 10.5281/zenodo.12795328. All images are in tif format.

Supporting Information

The Supporting Information is available free of charge at https://pubs.acs.org/doi/10.1021/acsphotonics.4c00337.

https://doi.org/10.1021/acsphotonics.4c00337
ACS Photonics 2024, 11, 3536−3544

Additional methods about p-SHG (theoretical background and image processing); median value of the order metrics of collagen orientation (entropy, circular variance, kurtosis, skewness) for all the mice under study; typical imaging data for NP, D6, D12, D15, and D18 mice; and maps and quantitation of entropy and kurtosis (PDF)

AUTHOR INFORMATION

Corresponding Authors

Jessica C. Ramella-Roman − *Biomedical Engineering Department, Florida International University, Miami, Florida 33174, United States;* orcid.org/0000-0002-5710-6004; Email: jramella@fiu.edu

Marie-Claire Schanne-Klein − *Laboratory for Optics and Biosciences (LOB), École Polytechnique, CNRS, Inserm, Institut Polytechnique de Paris, Palaiseau 91120, France;* orcid.org/0000-0003-3026-8932; Email: marie-claire.schanne-klein@polytechnique.edu

Authors

Mala Mahendroo − *Department of Obstetrics and Gynecology, University of Texas Southwestern Medical Center, Dallas, Texas 75390, United States*

Clothilde Raoux − *Laboratory for Optics and Biosciences (LOB), École Polytechnique, CNRS, Inserm, Institut Polytechnique de Paris, Palaiseau 91120, France*

Gaël Latour − *Laboratory for Optics and Biosciences (LOB), École Polytechnique, CNRS, Inserm, Institut Polytechnique de Paris, Palaiseau 91120, France; Université Paris-Saclay, Gif-sur-Yvette 91190, France*

Complete contact information is available at: https://pubs.acs.org/10.1021/acsphotonics.4c00337

Author Contributions

J.R.-R. and M.-C.S.-K. designed the study. J.R.-R., M.M., G.L., and M.-C.S.-K. designed the experimental protocols. J.R.-R., C.R., and M.-C.S.-K. designed the numerical analyses. J.R.-R. acquired and analyzed all the data with contributions from M.-C.S.-K. J.R.-R., M.-C.S.-K, and M.M. wrote the manuscript. All authors read, corrected, and approved the final manuscript.

Funding

J.R.-R. acknowledge partial support from the Wertheim foundation, NSF grant #1548924 STROBE and the "Invited Professors" program from Ecole Polytechnique, France. M.-C.S.-K., G.L. and C.R. acknowledge funding from the French "Agence Nationale de la Recherche" (ANR-10-INBS-04, ANR-11-EQPX-0029).

Notes

The authors declare no competing financial interest.

Code availability: A Matlab script used to calculate entropy, variance and kurtosis is provided at https://github.com/jramella/ACS_PHOTONICS.

ACKNOWLEDGMENTS

The authors acknowledge the support of Ajmal and Mariano Colon Caraballo in the preparation of some of the cervical samples. They also thank Xavier Solinas and Jean-Marc Sintès for technical support in the SHG setup and Tatiana Novikova and the "Advanced microscopies group" at LOB for fruitful discussions.

REFERENCES

(1) Garfield, R. E.; Maul, H.; Shi, L.; Maner, W.; Fittkow, C.; Olsen, G.; Saade, G. R. Methods and devices for the management of term and preterm labor. *Ann. N.Y. Acad. Sci.* **2001**, *943*, 203−224.

(2) Soleimani, F.; Zaheri, F.; Abdi, F. Long-term neurodevelopmental outcomes after preterm birth. *Iran. Red Crescent Med. J.* **2014**, *16* (6), No. e17965.

(3) Saigal, S.; Doyle, L. An overview of mortality and sequelae of preterm birth from infancy to adulthood. *Lancet* **2008**, *371* (9608), 261−269.

(4) Shapiro-Mendoza, C. K.; Barfield, W. D.; Henderson, Z.; James, A.; Howse, J. L.; Iskander, J.; Thorpe, P. G. CDC grand rounds: public health strategies to prevent preterm birth. *MMWR Morb. Mortal. Wkly. Rep.* **2016**, *65* (32), 826−830.

(5) Blumenshine, P.; Egerter, S.; Barclay, C. J.; Cubbin, C.; Braveman, P. A. Socioeconomic disparities in adverse birth outcomes: a systematic review. *Am. J. Prev. Med.* **2010**, *39* (3), 263−272.

(6) Mehra, R.; Keene, D. E.; Kershaw, T. S.; Ickovics, J. R.; Warren, J. L. Racial and ethnic disparities in adverse birth outcomes: differences by racial residential segregation. *SSM Popul. Health* **2019**, *8*, 100417.

(7) Beck, A. F.; Edwards, E. M.; Horbar, J. D.; Howell, E. A.; McCormick, M. C.; Pursley, D. M. The color of health: how racism, segregation, and inequality affect the health and well-being of preterm infants and their families. *Pediatr. Res.* **2020**, *87* (2), 227−234.

(8) Zork, N. M.; Myers, K. M.; Yoshida, K.; Cremers, S.; Jiang, H.; Ananth, C. V.; Wapner, R. J.; Kitajewski, J.; Vink, J. A systematic evaluation of collagen cross-links in the human cervix. *Am. J. Obstet. Gynecol.* **2015**, *212* (3), 321.e1−321.e8.

(9) Fernandez, M.; House, M.; Jambawalikar, S.; Zork, N.; Vink, J.; Wapner, R.; Myers, K. Investigating the mechanical function of the cervix during pregnancy using finite element models derived from high-resolution 3D MRI. *Comput. Methods Biomech. Biomed. Eng.* **2016**, *19* (4), 404−417.

(10) Myers, K. M.; Feltovich, H.; Mazza, E.; Vink, J.; Bajka, M.; Wapner, R. J.; Hall, T. J.; House, M. The mechanical role of the cervix in pregnancy. *J. Biomech.* **2015**, *48* (9), 1511−1523.

(11) Akins, M. L.; Luby-Phelps, K.; Mahendroo, M. Second harmonic generation imaging as a potential tool for staging pregnancy and predicting preterm birth. *J. Biomed. Opt.* **2010**, *15* (2), 026020.

(12) Read, C. P.; Word, R. A.; Ruscheinsky, M. A.; Timmons, B. C.; Mahendroo, M. S. Cervical remodeling during pregnancy and parturition: molecular characterization of the softening phase in mice. *Reproduction* **2007**, *134* (2), 327−340.

(13) Cunningham, F. G.; Williams, J. W.. *Williams Obstetrics*, 23rd ed.; McGraw-Hill Medical: New York, 2010.

(14) Romero, R.; Espinoza, J.; Kusanovic, J. P.; Gotsch, F.; Hassan, S.; Erez, O.; Chaiworapongsa, T.; Mazor, M. The preterm parturition syndrome. *BJOG: An Int. J. Obstet. Gynaecol.* **2006**, *113* (s3), 17−42.

(15) Nallasamy, S.; Palacios, H. H.; Setlem, R.; Colon Caraballo, M.; Li, K.; Cao, E.; Shankaran, M.; Hellerstein, M.; Mahendroo, M. Transcriptome and proteome dynamics of cervical remodeling in the mouse during pregnancy. *Biol. Reprod.* **2021**, *105* (5), 1257−1271.

(16) Yoshida, K.; Jiang, H.; Kim, M.; Vink, J.; Cremers, S.; Paik, D.; Wapner, R.; Mahendroo, M.; Myers, K. Quantitative evaluation of collagen crosslinks and corresponding tensile mechanical properties in mouse cervical tissue during normal pregnancy. *PLoS One* **2014**, *9* (11), No. e112391.

(17) Akins, M. L.; Luby-Phelps, K.; Bank, R. A.; Mahendroo, M. Cervical softening during pregnancy: regulated changes in collagen cross-linking and composition of matricellular proteins in the mouse. *Biol. Reprod.* **2011**, *84* (5), 1053−1062.

(18) Blaustein, A.; Kurman, K. J. *Blaustein's Pathology of the Female Genital Tract*; Springer US: New York, NY, 2011.

(19) House, M.; Kaplan, D. L.; Socrate, S. Relationships between mechanical properties and extracellular matrix constituents of the cervical stroma during pregnancy. *Semin. Perinatol.* **2009**, *33* (5), 300−307.

(20) Myers, K.; Socrate, S.; Tzeranis, D.; House, M. Changes in the biochemical constituents and morphologic appearance of the human cervical stroma during pregnancy. *Eur. J. Obstet. Gynecol. Reprod. Biol.* **2009**, *144*, S82−S89.
(21) Yao, W.; Gan, Y.; Myers, K. M.; Vink, J. Y.; Wapner, R. J.; Hendon, C. P. Collagen fiber orientation and dispersion in the upper cervix of non-pregnant and pregnant women. *PLoS One* **2016**, *11* (11), No. e0166709.
(22) Granstrom, L.; Ekman, G.; Ulmsten, U.; Malmstrom, A. Changes in the connective tissue of corpus and cervix uteri during ripening and labour in term pregnancy. *Br. J. Obstet. Gynaecol.* **1989**, *96* (10), 1198−1202.
(23) Sennstrom, M. B.; Ekman, G.; Westergren-Thorsson, G.; Malmstrom, A.; Bystrom, B.; Endresen, U.; Mlambo, N.; Norman, M.; Ståbi, B.; Brauner, A. Human cervical ripening, an inflammatory process mediated by cytokines. *Mol. Hum. Reprod.* **2000**, *6* (4), 375−381.
(24) Osmers, R.; Rath, W.; Pflanz, M. A.; Kuhn, W.; Stuhlsatz, H. W.; Szeverenyi, M. Glycosaminoglycans in cervical connective tissue during pregnancy and parturition. *Obstet. Gynecol.* **1993**, *81* (1), 88−92.
(25) Shi, L.; Shi, S. Q.; Saade, G. R.; Chwalisz, K.; Garfield, R. E. Changes in cervical resistance and collagen fluorescence during gestation in rats. *J. Perinat. Med.* **1999**, *27* (3), 188−194.
(26) Maul, H.; Olson, G.; Fittkow, C. T.; Saade, G. R.; Garfield, R. E. Cervical light-induced fluorescence in humans decreases throughout gestation and before delivery: preliminary observations. *Am. J. Obstet. Gynecol.* **2003**, *188* (2), 537−541.
(27) Bancelin, S.; Nazac, A.; Ibrahim, B. H.; Dokladal, P.; Decenciere, E.; Teig, B.; Haddad, H.; Fernandez, H.; Schanne-Klein, M. C.; De Martino, A. Determination of collagen fiber orientation in histological slides using Mueller microscopy and validation by second harmonic generation imaging. *Opt. Express* **2014**, *22* (19), 22561−22574.
(28) Word, R. A.; Li, X. H.; Hnat, M.; Carrick, K. Dynamics of cervical remodeling during pregnancy and parturition: mechanisms and current concepts. *Semin. Reprod. Med.* **2007**, *25* (1), 069−079.
(29) Holt, R.; Timmons, B. C.; Akgul, Y.; Akins, M. L.; Mahendroo, M. The molecular mechanisms of cervical ripening differ between term and preterm birth. *Endocrinology* **2011**, *152* (3), 1036−1046.
(30) Reusch, L. M.; Feltovich, H.; Carlson, L. C.; Hall, G.; Campagnola, P. J.; Eliceiri, K. W.; Hall, T. J. Nonlinear optical microscopy and ultrasound imaging of human cervical structure. *J. Biomed. Opt.* **2013**, *18* (3), 031110.
(31) Myers, K. M.; Socrate, S.; Paskaleva, A.; House, M. A study of the anisotropy and tension/compression behavior of human cervical tissue. *J. Biomech. Eng.* **2010**, *132* (2), 021003.
(32) Aspden, R. M. Collagen organisation in the cervix and its relation to mechanical function. *Collagen Relat. Res.* **1988**, *8* (2), 103−112.
(33) Nott, J. P.; Pervolaraki, E.; Benson, A. P.; Bonney, E. A.; Pickering, J. D.; Wilkinson, N.; Simpson, N. Diffusion tensor imaging determines three-dimensional architecture of human cervix: a cross-sectional study. *BJOG: An Int. J. Obstet. Gynaecol.* **2018**, *125* (7), 812−818.
(34) Guerrero, Q. W.; Feltovich, H.; Rosado-Mendez, I. M.; Carlson, L. C.; Li, G.; Hall, T. J. Anisotropy and spatial heterogeneity in quantitative ultrasound parameters: relevance to the study of the human cervix. *Ultrasound Med. Biol.* **2018**, *44* (7), 1493−1503.
(35) Gan, Y.; Yao, W.; Myers, K. M.; Vink, J. Y.; Wapner, R. J.; Hendon, C. P. Analyzing three-dimensional ultrastructure of human cervical tissue using optical coherence tomography. *Biomed. Opt. Express* **2015**, *6* (4), 1090−1108.
(36) Chue-Sang, J.; Bai, Y.; Stoff, S.; Gonzalez, M.; Holness, N.; Gomes, J.; Jung, R.; Gandjbakhche, A.; Chernomordik, V. V.; Ramella-Roman, J. C. Use of Mueller matrix polarimetry and optical coherence tomography in the characterization of cervical collagen anisotropy. *J. Biomed. Opt.* **2017**, *22* (08), 1−9.
(37) Chue-Sang, J.; Holness, N.; Gonzalez, M.; Greaves, J.; Saytashev, I.; Stoff, S.; Gandjbakhche, A.; Chernomordik, V.; Burkett, G.; Ramella-Roman, J. Use of Mueller matrix colposcopy in the characterization of cervical collagen anisotropy. *J. Biomed. Opt.* **2018**, *23* (12), 1−9.
(38) Pierangelo, A.; Vizet, J.; Rehbinder, J.; Nazac, A. Method and apparatus for quantifying the progression of a pregnancy. EP 3766403 A1, 2021.
(39) O'Brien, C. M.; Vargis, E.; Rudin, A.; Slaughter, J. C.; Thomas, G.; Newton, J. M.; Reese, J.; Bennett, K. A.; Mahadevan-Jansen, A. In vivo Raman spectroscopy for biochemical monitoring of the human cervix throughout pregnancy. *Am. J. Obstet. Gynecol.* **2018**, *218* (5), 528.e1−528.e18.
(40) Feltovich, H.; Hall, T. J.; Berghella, V. Beyond cervical length: emerging technologies for assessing the pregnant cervix. *Am. J. Obstet. Gynecol.* **2012**, *207* (5), 345−354.
(41) Zhang, Y.; Akins, M. L.; Murari, K.; Xi, J.; Li, M. J.; Luby-Phelps, K.; Mahendroo, M.; Li, X. A compact fiber-optic SHG scanning endomicroscope and its application to visualize cervical remodeling during pregnancy. *Proc. Natl. Acad. Sci. U.S.A.* **2012**, *109* (32), 12878−12883.
(42) Lau, T. Y.; Sangha, H. K.; Chien, E. K.; McFarlin, B. L.; Wagoner Johnson, A. J.; Toussaint, K. C., Jr. Application of Fourier transform-second-harmonic generation imaging to the rat cervix. *J. Microsc.* **2013**, *251* (1), 77−83.
(43) Chen, X. Y.; Nadiarynkh, O.; Plotnikov, S.; Campagnola, P. J. Second harmonic generation microscopy for quantitative analysis of collagen fibrillar structure. *Nat. Protoc.* **2012**, *7* (4), 654−669.
(44) Bancelin, S.; Aimé, C.; Gusachenko, I.; Kowalczuk, L.; Latour, G.; Coradin, T.; Schanne-Klein, M.-C. Determination of collagen fibril size via absolute measurements of second-harmonic generation signals. *Nat. Commun.* **2014**, *5*, 4920.
(45) Moghaddam, A. O.; Lin, Z.; Sivaguru, M.; Phillips, H.; McFarlin, B. L.; Toussaint, K. C.; Johnson, A. W. Heterogeneous microstructural changes of the cervix influence cervical funneling. *Acta Biomater.* **2022**, *140*, 434−445.
(46) Stoller, P.; Reiser, K. M.; Celliers, P. M.; Rubenchik, A. M. Polarization-modulated second harmonic generation in collagen. *Biophys. J.* **2002**, *82* (6), 3330−3342.
(47) Tiaho, F.; Recher, G.; Rouède, D. Estimation of helical angles of myosin and collagen by second harmonic generation imaging microscopy. *Opt. Express* **2007**, *15* (19), 12286−12295.
(48) Tuer, A. E.; Akens, M. K.; Krouglov, S.; Sandkuijl, D.; Wilson, B. C.; Whyne, C. M.; Barzda, V. Hierarchical model of fibrillar collagen organization for interpreting the second-order susceptibility tensors in biological tissue. *Biophys. J.* **2012**, *103* (10), 2093−2105.
(49) Gusachenko, I.; Tran, V.; Houssen, Y.; Allain, J.-M.; Schanne-Klein, M.-C. Polarization-resolved second-harmonic generation in tendon upon mechanical stretching. *Biophys. J.* **2012**, *102* (9), 2220−2229.
(50) Duboisset, J.; Ait-Belkacem, D.; Roche, M.; Rigneault, H.; Brasselet, S. Generic model of the molecular orientational distribution probed by polarization-resolved second-harmonic generation. *Phys. Rev. A* **2012**, *85* (4), 043829.
(51) Raoux, C.; Chessel, A.; Mahou, P.; Latour, G.; Schanne-Klein, M. C. Unveiling the lamellar structure of the human cornea over its full thickness using polarization-resolved SHG microscopy. *Light Sci. Appl.* **2023**, *12* (1), 190.
(52) Liu, Y. M.; Keikhosravi, A.; Mehta, G. S.; Drifka, C. R.; Eliceiri, K. W. Methods for quantifying fibrillar collagen alignment. *Methods Mol. Biol.* **2017**, *1627*, 429−451.
(53) Liu, Z.; Pouli, D.; Sood, D.; Sundarakrishnan, A.; Hui Mingalone, C. K.; Arendt, L. M.; Alonzo, C.; Quinn, K. P.; Kuperwasser, C.; Zeng, L.; Schnelldorfer, T.; Kaplan, D. L.; Georgakoudi, I. Automated quantification of three-dimensional organization of fiber-like structures in biological tissues. *Biomaterials* **2017**, *116*, 34−47.
(54) Zipfel, W. R.; Williams, R. M.; Christie, R.; Nikitin, A. Y.; Hyman, B. T.; Webb, W. W. Live tissue intrinsic emission microscopy

https://doi.org/10.1021/acsphotonics.4c00337
ACS Photonics 2024, 11, 3536−3544

using multiphoton-excited native fluorescence and second harmonic generation. *Proc. Natl. Acad. Sci. U.S.A.* **2003**, *100* (12), 7075−7080.
(55) Yoshida, K.; Jayyosi, C.; Lee, N.; Mahendroo, M.; Myers, K. M. Mechanics of cervical remodelling: insights from rodent models of pregnancy. *Interface Focus* **2019**, *9* (5), 20190026.
(56) Couture, C. A.; Bancelin, S.; Van der Kolk, J.; Popov, K.; Rivard, M.; Legare, K.; Martel, G.; Richard, H.; Brown, C.; Laverty, S.; Ramunno, L.; Legare, F. The impact of collagen fibril polarity on second harmonic generation microscopy. *Biophys. J.* **2015**, *109* (12), 2501−2510.
(57) Raanan, D.; Song, M. S.; Tisdale, W. A.; Oron, D. Super-resolved second harmonic generation imaging by coherent image scanning microscopy. *Appl. Phys. Lett.* **2022**, *120* (7), 071111.
(58) Roa, C.; Du Le, V. N.; Mahendroo, M.; Saytashev, I.; Ramella-Roman, J. C. Auto-detection of cervical collagen and elastin in Mueller matrix polarimetry microscopic images using K-NN and semantic segmentation classification. *Biomed. Opt. Express* **2021**, *12* (4), 2236−2249.
(59) Lee, H. R.; Saytashev, I.; Du Le, V. N.; Mahendroo, M.; Ramella-Roman, J.; Novikova, T. Mueller matrix imaging for collagen scoring in mice model of pregnancy. *Sci. Rep.* **2021**, *11* (1), 15621.
(60) Morizet, J.; Ducourthial, G.; Supatto, W.; Boutillon, A.; Legouis, R.; Schanne-Klein, M. C.; Stringari, C.; Beaurepaire, E. High-speed polarization-resolved third-harmonic microscopy. *Optica* **2019**, *6* (3), 385−388.
(61) Ducourthial, G.; Affagard, J.-S.; Schmeltz, M.; Solinas, X.; Lopez-Poncelas, M.; Bonod-Bidaud, C.; Rubio-Amador, R.; Ruggiero, F.; Allain, J.-M.; Beaurepaire, E.; Schanne-Klein, M.-C. Monitoring dynamic collagen reorganization during skin stretching with fast polarization-resolved second harmonic generation imaging. *J. Biophot.* **2019**, *12* (5), No. e201800336.
(62) Shi, L.; Yao, W.; Gan, Y.; Zhao, L. Y.; Eugene McKee, W.; Vink, J.; Wapner, R. J.; Hendon, C. P.; Myers, K. Anisotropic material characterization of human cervix tissue based on indentation and inverse finite element analysis. *J. Biomech. Eng.* **2019**, *141* (9), 0910171−09101713.
(63) Shi, L.; Hu, L.; Lee, N.; Fang, S.; Myers, K. Three-dimensional anisotropic hyperelastic constitutive model describing the mechanical response of human and mouse cervix. *Acta Biomater.* **2022**, *150*, 277−294.
(64) Schmeltz, M.; Teulon, C.; Pinsard, M.; Hansen, U.; Alnawaiseh, M.; Ghoubay, D.; Borderie, V.; Mosser, G.; Aimé, C.; Légaré, F.; Latour, G.; Schanne-Klein, M. C. Circular-dichroism SHG microscopy probes the polarity distribution of out-of-plane collagen fibril assemblies. In *2021 Conference on Lasers and Electro-Optics Europe & European Quantum Electronics Conference (Cleo/Europe-Eqec)*, 2021.
(65) Raoux, C.; Schmeltz, M.; Bied, M.; Alnawaiseh, M.; Hansen, U.; Latour, G.; Schanne-Klein, M.-C. Quantitative structural imaging of keratoconic corneas using polarization-resolved SHG microscopy. *Biomed. Opt. Express* **2021**, *12* (7), 4163−4178.
(66) Boyd, R. W. *Nonlinear Optics*; Academic Press: London, 2003.
(67) Schmeltz, M.; Robinet, L.; Heu-Thao, S.; Sintes, J. M.; Teulon, C.; Ducourthial, G.; Mahou, P.; Schanne-Klein, M. C.; Latour, G. Noninvasive quantitative assessment of collagen degradation in parchments by polarization-resolved SHG microscopy. *Sci. Adv.* **2021**, *7* (29), No. eabg1090.
(68) Preibisch, S.; Saalfeld, S.; Tomancak, P. Globally optimal stitching of tiled 3D microscopic image acquisitions. *Bioinformatics* **2009**, *25* (11), 1463−1465.
(69) Fisher, N. *Statistical Analysis of Circular Data*; Cambridge University Press, 1993.

https://doi.org/10.1021/acsphotonics.4c00337
ACS Photonics 2024, 11, 3536−3544

Quantitative assessment of collagen remodeling during murine pregnancy

Jessica C. Ramella-Roman[a], Mala Mahendroo[b], Clothilde Raoux[c], Gaël Latour[c,d], Marie-Claire Schanne-Klein[c]

a. Biomedical Engineering Department, Florida International University, Miami, FL 33174 United States
b. Department of Obstetrics and Gynecology, University of Texas Southwestern Medical Center, Dallas, Texas 75390, USA
c. Laboratory for Optics and Biosciences (LOB), École Polytechnique, CNRS, Inserm, Institut Polytechnique de Paris, 91120, Palaiseau, France
d. Université Paris-Saclay, 91190 Gif-sur-Yvette, France

Supplementary Methods

Polarization-resolved SHG (p-SHG) theoretical background

Second Harmonic Generation (SHG) is a multiphoton modality that is complementary to 2-photon excited fluorescence (2PEF). It appears at exactly half the excitation wavelength and is specific to dense and non-centrosymmetric materials[1]. At the molecular level, the main so-called "harmonophore" in biological tissues is the peptide bond because it exhibits delocalized π electrons in a non-centrosymmetric environment that behave as a nonlinear dipole at the harmonic frequency[2-5]. Tight alignment of these peptide bonds within collagen triple helices and fibrils results in a detectable SHG signal that is specific to the dense and non centro-symmetric fibrillar organization of collagen. SHG microscopy thus allows 3D imaging of collagen at the micrometer scale without any staining and with unprecedented contrast. In practice, SHG can be excited at any wavelength in the red-near infrared range. It can be spectrally separated from the Stokes-shifted 2PEF signals using dichroic mirrors.

Most interestingly, the SHG signal of fibrillar collagen depends on the orientation of the collagen fibril to the polarization angle of the laser excitation. Recording series of SHG images when varying the polarization orientation of a linearly-polarized laser thus enables the determination of the collagen orientation in every pixel, independently of the neighboring pixels. It relies on a theoretical analysis of the variation of the SHG signal as a function of the excitation polarization. This analysis of the so-called p-SHG signal is performed in the framework of tensorial nonlinear optics[1]. SHG is described theoretically by a susceptibility tensor $\chi^{(2)}$, which exhibits the symmetry of the material under study. Considering the cylindrical symmetry of collagen fibrils and assuming that Kleinman symmetry is valid because of the non-resonant excitation, there are only 2 non zero independent tensorial components:[6] $\chi^{(2)}_{XXX}$ and $\chi^{(2)}_{XYY} = \chi^{(2)}_{XZZ} = \chi^{(2)}_{YXY} = \chi^{(2)}_{ZXZ} = \chi^{(2)}_{YYX} = \chi^{(2)}_{ZZX}$. We define the anisotropy parameter as: $\rho = \chi_{XXX}/\chi_{XYY}$, which has been measured as $\rho \approx 1.4$[3, 7]. The induced second harmonic polarization then writes[1]:

$$P_I^{(2)}(\vec{r}) = \epsilon_0 \sum_{J,K} \chi^{(2)}_{IJK} E_J(\vec{r}) E_K(\vec{r}) \quad \text{(S1)}$$

Here *I,J,K* refer to the Cartesian components of the fields and $\vec{E}(\vec{r},t) = \vec{E}(\vec{r})\, e^{-i\omega t} + cc$ is the excitation electric field at frequency ω. Let's consider a linearly-polarized excitation laser at angle θ to the axis X in the microscope frame (X,Y,Z):

$$\vec{E}(\vec{r}) = E_0 e^{ikZ} \begin{pmatrix} cos\,\theta \\ sin\,\theta \\ 0 \end{pmatrix}_{(X,Y,Z)} \quad \text{(S2)}$$

Eq. (2) is written in the plane wave approximation and neglects the axial electric field component along the microscope axis Z due to strong focusing. We have indeed shown previously that strong focusing does not affect the determination of the in-plane orientation φ of collagen fibrils[8]. The SHG signal intensity is then obtained from the square modulus of the nonlinear polarization. Summing the X- and Y-polarized contributions, one gets [9-13]:

$$I_{SHG}(\theta) = C\, {I_\omega}^2 \left[\left(\rho\, cos^2(\theta-\varphi) + sin^2(\theta-\varphi)\right)^2 + (sin2(\theta-\varphi))^2\right] \quad \text{(S3)}$$

Here I_ω is the intensity of the excitation laser and C is a parameter merging geometrical and other parameters. Note that the expression of ρ is modified for collagen fibrils oriented out of the imaging plane or a disordered assembly of fibrils within the focal volume, resulting in a higher value[13]. Nevertheless, Eq. (S3) still applies and φ corresponds to the main orientation in the imaging plane of the fibril assembly.

Eq. (S3) describes the p-SHG response in every pixel and well reproduces the experimental data as exemplified in Fig. S4. Fig. S4.a displays SHG images recorded at different excitation polarization, which exhibit different intensities as expected. The p-SHG response in a small region of interest is plotted in Fig. S4.b (black solid dots) and well fitted with Eq. (S3) (red solid line). It exhibits 2 maxima and 2 minima in the [0, 180°] range: the main fibril orientation φ is given by the first minimum and the anisotropy parameter is given by the square root of the 2 minima (orange and blue solid dots in Figure S4.b). Note that SHG is not sensitive to the polarity of the fibrils, so that this polarimetric diagram is symmetric in the [0, 180°] and [180°, 360°] ranges.

Efficient pixel-by-pixel processing of p-SHG data is obtained by an automated Fast Fourier Transform (FFT) analysis. Eq. (S3) is thus expressed as its Fourier components as follows:

$$I_{SHG}(\theta) = \; a_0 + a_2\, cos[2(\theta-\varphi)] \; + \; a_4\, cos[4(\theta-\varphi)] \quad \text{(S4)}$$

a_0, a_2 and a_4 are functions of the collagen susceptibility tensor components and of the square modulus of the excitation intensity, as well as other geometrical or experimental parameters. They provide 4 parameters as described in the main text[13]. As FFT processing of experimental p-SHG data results in complex parameters α_0, α_2 and α_4, the fibril orientation φ is processed as a weighted average of the phases of the 2nd and 4st Fourier components (α_2 and α_4). The coefficient of determination R^2 is calculated as follows:

$$R^2 = \max\left(0, 1 - \frac{\sum_\theta [I_{SHG}(\theta) - I_{FFT}(\theta)]^2}{\sum_\theta [I_{SHG}(\theta) - \langle I_{SHG}(\theta)\rangle]^2}\right) \quad \text{(S5)}$$

where $$I_{FFT}(\theta) = \alpha_0 + \alpha_2 e^{2i\theta} + \alpha_4 e^{4i\theta} \; + \; c.c. \quad \text{(S6)}$$

Supplementary Table

Mouse	Entropy	Circ. variance	Circ. kurtosis	Circ. skewness
NP-a	0.644	0.218	0.474	0.000
NP-b	0.690	0.280	0.396	0.002
NP-c	0.625	0.176	0.532	0.000
D6-a	0.645	0.181	0.524	0.001
D6-b	0.598	0.142	0.599	0.001
D6-c	0.614	0.216	0.480	0.000
D12-a	0.616	0.169	0.550	0.000
D12-b	0.592	0.159	0.570	0.000
D12-c	0.647	0.227	0.471	0.000
D15-a	0.714	0.330	0.358	-0.001
D15-b	0.678	0.313	0.377	-0.001
D15-c	0.639	0.254	0.440	-0.002
D18-a	0.707	0.329	0.356	0.000
D18-b	0.770	0.431	0.261	0.000
D18-c	0.731	0.345	0.336	0.001

Table T1: Median value of the order metrics of collagen orientation for all the mice under study.

Supplementary Figures

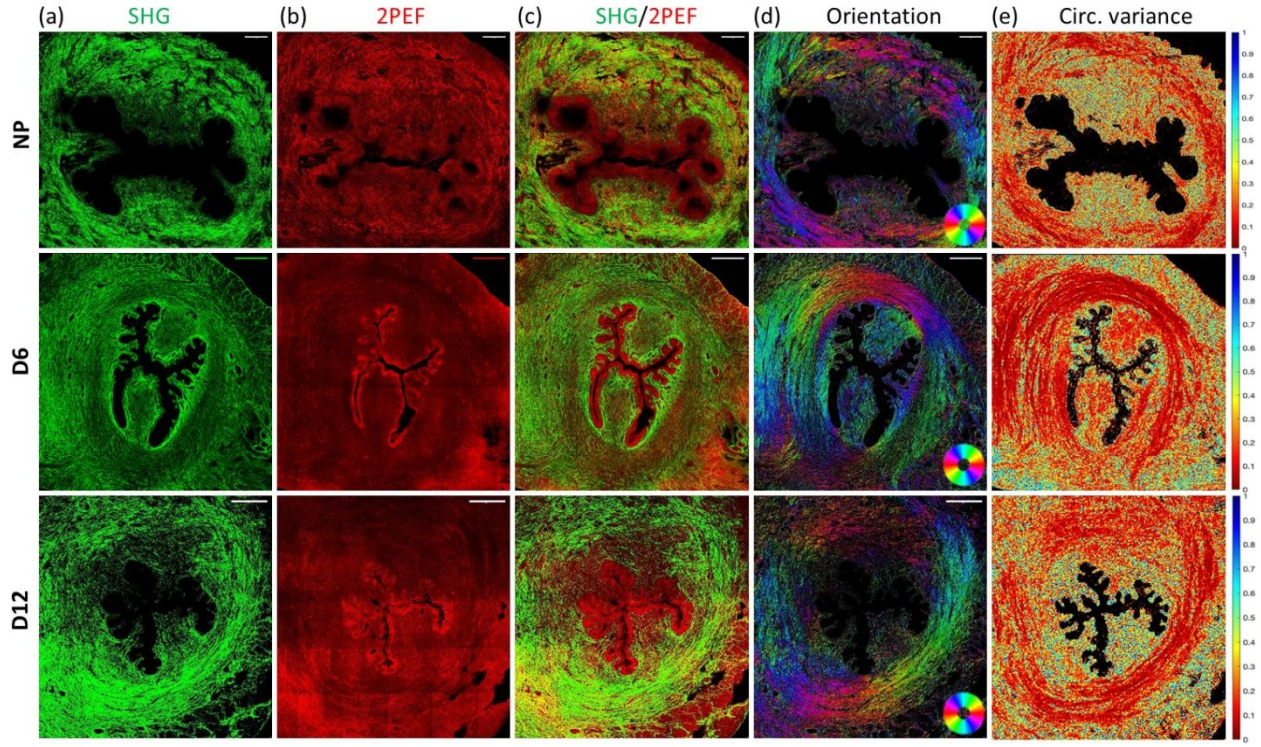

Figure S1: typical imaging data for NP (top), D6 (middle) and D12 (bottom) mice. (a) I_{SHG} image, (b) I_{2PEF} image, (c) Combined I_{2PEF} (red color) and I_{SHG} (green color) image, (d) Orientation map of collagen fibers extracted from pSHG data. HSV look-up table is used: H codes the collagen orientation (see colored wheel), S=1 and V=R^2 for R^2>0.5, V=0 otherwise. (e) Circular variance of the orientation distribution from 10 x10 pixels ROIs. Scale bars: 200 µm.

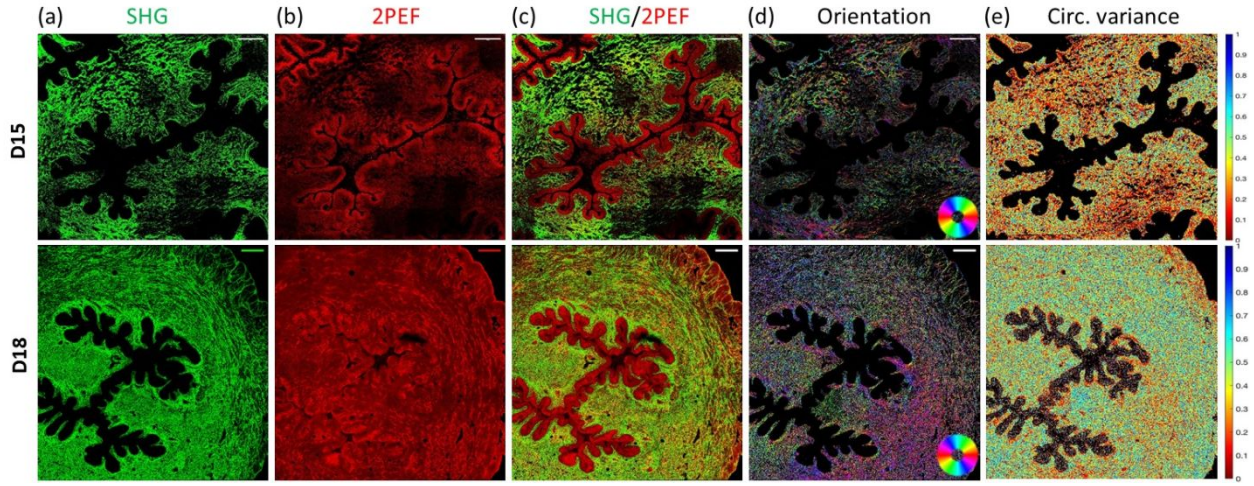

Figure S2: typical imaging data for D15 (top) and D18 (bottom) mice. (a) I_{SHG} image, (b) I_{2PEF} image, (c) Combined I_{2PEF} (red color) and I_{SHG} (green color) image, (d) Orientation map of collagen fibers extracted from pSHG data. HSV look-up table is used: H codes the collagen orientation (see colored wheel), S=1 and V=R^2 for R^2>0.5, V=0 otherwise. (e) Circular variance of the orientation distribution from 10 x10 pixels ROIs. Scale bars: 200 µm.

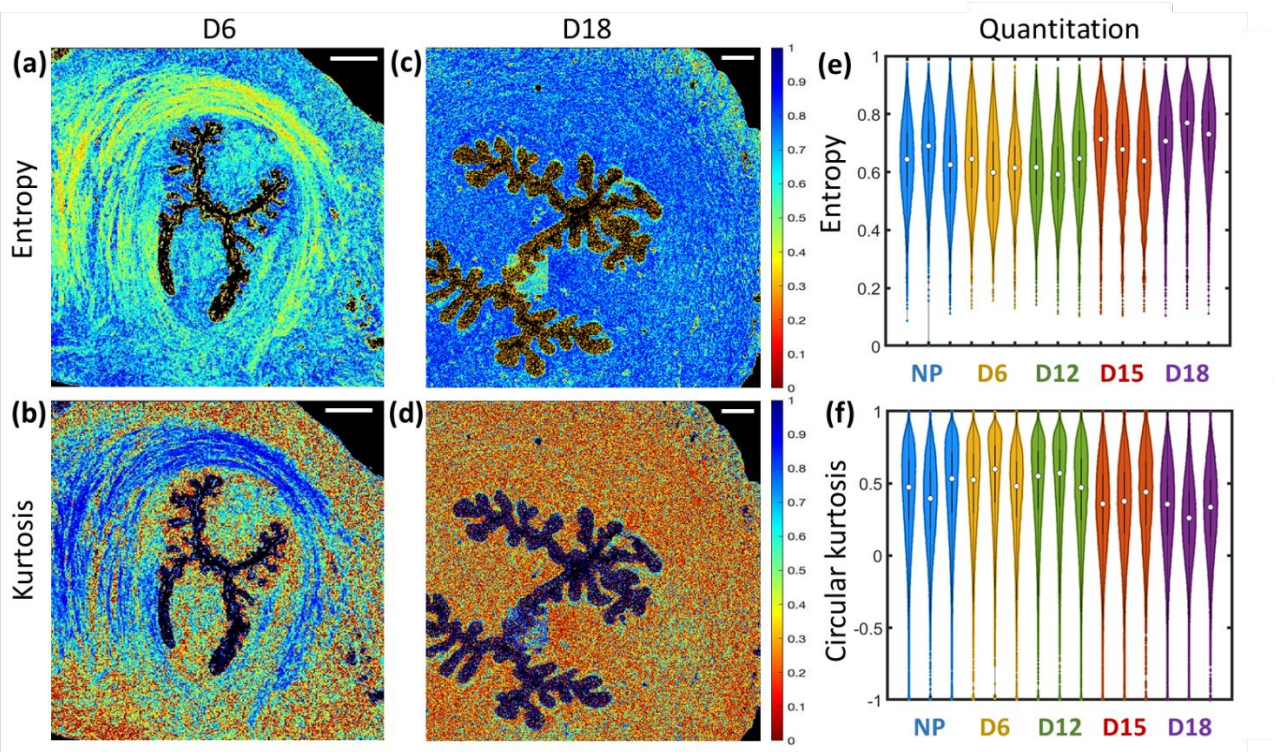

Figure S3: Order metrics of collagen orientation. The entropy is 0 for a perfectly ordered distribution and 1 for a completely random one. The kurtosis is higher when the distribution is more tailed. (a, d) Map of the (a, c) entropy and of the (b,d) kurtosis calculated in small ROIs spanning the pSHG orientation image of the same (a, b) D6 and (c, d) D18 samples as in figs 2 and 3. (e,f) Violin plots of the (e) entropy and of the (f) kurtosis calculated in all the ROIs spanning the cervix for all samples under study. Each column represents a different sample from a different mouse. Median (white dot) and interquartile line (black bold line) are plotted for every column. In every sample, the edges are eliminated by an elliptical mask covering the os. Scale bar: 200 µm.

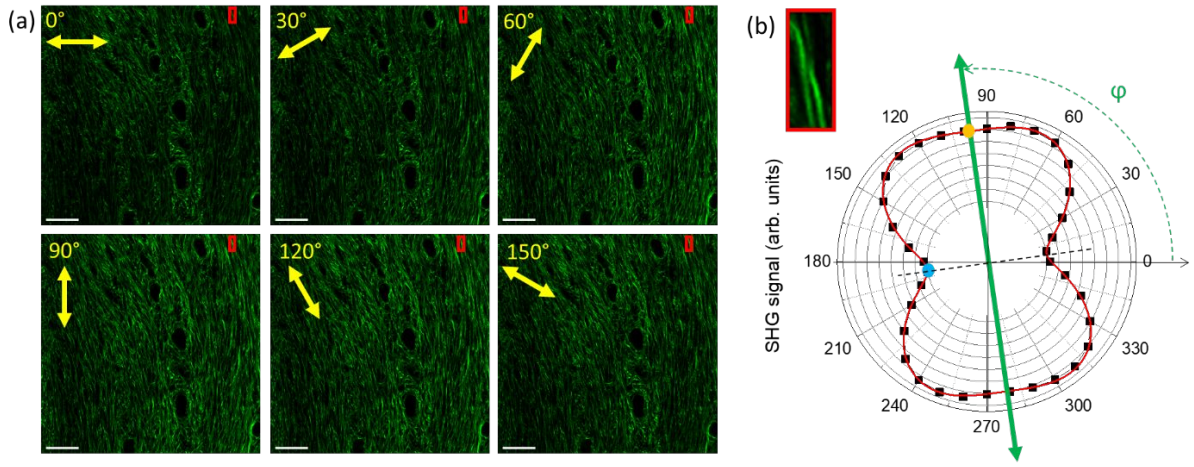

Figure S4: p-SHG imaging and analysis. (a) SHG images of the same tile recorded for different excitation polarization orientations, indicated in yellow color. (b) Angular plot of the experimental SHG signal (black solid squares) in the red rectangles in (a). The red solid line is a fit using Eq. (S3), which gives the main fibril orientation φ along the first minimum (green double arrow). The anisotropy parameter is given by the square root of the 2 minima (orange and blue solid dots). Note that the same process can be applied to a single pixel. Here a small region of interest is processed to obtain a better signal to noise ratio and to facilitate comparison with the orientation in the image. Scale bar: 50 µm.

References

1. Boyd, R. W., *Nonlinear optics*. Academic press: London, 2003.
2. Plotnikov, S. V.; Millard, A. C.; Campagnola, P. J.; Mohler, W. A., Characterization of the myosin-based source for second-harmonic generation from muscle sarcomeres. *Biophys. J.* **2006,** *90*, 693–703.
3. Tiaho, F.; Recher, G.; Rouède, D., Estimation of helical angle of myosin and collagen by second harmonic generation imaging microscopy *Opt. Express* **2007,** *15* (19), 12286-12295.
4. Duboisset, J.; Deniset-Besseau, A.; Benichou, E.; Russier-Antoine, I.; Lascoux, N.; Jonin, C.; Hache, F.; Schanne-Klein, M.-C.; Brevet, P.-F., A Bottom-Up Approach to Build the Hyperpolarizability of Peptides and Proteins from their Amino-Acids. *J. Phys. Chem. B* **2013,** *117* (34), 9877-9881.
5. Bancelin, S.; Aimé, C.; Gusachenko, I.; Kowalczuk, L.; Latour, G.; Coradin, T.; Schanne-Klein, M.-C., Determination of collagen fibril size via absolute measurements of second-harmonic generation signals. *Nat. Commun.* **2014,** *5*, 4920.
6. Stoller, P.; Reiser, K. M.; Celliers, P. M.; Rubenchik, A. M., Polarization-modulated second harmonic generation in collagen. *Biophys J.* **2002,** *82* (6), 3330-3342.
7. Teulon, C.; Gusachenko, I.; Latour, G.; Schanne-Klein, M.-C., Theoretical, numerical and experimental study of geometrical parameters that affect anisotropy measurements in polarization-resolved SHG microscopy. *Opt. Express* **2015,** *23* (7), 9313-9328.
8. Gusachenko, I.; Schanne-Klein, M.-C., Numerical simulation of polarization-resolved second harmonic microscopy in birefringent media. *Phys. Rev. A* **2013,** *88*, 053811.
9. Stoller, P.; Kim, B.-M.; Rubenchik, A. M.; Reiser, K. M.; Da Silva, L. B., Polarization-dependent optical second-harmonic imaging of a rat-tail tendon. *J. Biomed. Opt.* **2002,** *7* (2), 205-214.
10. Tuer, A. E.; Akens, M. K.; Krouglov, S.; Sandkuijl, D.; Wilson, B. C.; Whyne, C. M.; Barzda, V., Hierarchical Model of Fibrillar Collagen Organization for Interpreting the Second-Order Susceptibility Tensors in Biological Tissue. *Biophys. J.* **2012,** *103* (10), 2093-2105.
11. Duboisset, J.; Ait-Belkacem, D.; Roche, M.; Rigneault, H.; Brasselet, S., Generic model of the molecular orientational distribution probed by polarization-resolved second-harmonic generation. *Phys. Rev. A* **2012,** *85* (4), 043829.
12. Rouede, D.; Schaub, E.; Bellanger, J. J.; Ezan, F.; Scimeca, J. C.; Baffet, G.; Tiaho, F., Determination of extracellular matrix collagen fibril architectures and pathological remodeling by polarization dependent second harmonic microscopy. *Sci. Rep.* **2017,** *7,* 12197.
13. Raoux, C.; Schmeltz, M.; Bied, M.; Alnawaiseh, M.; Hansen, U.; Latour, G.; Schanne-Klein, M.-C., Quantitative structural imaging of keratoconic corneas using polarization-resolved SHG microscopy. *Biomed. Opt. Express* **2021,** *12* (7), 4163-4178.